Periodica Polytechnica Chemical Engineering, 69(4), pp. 510–524, 2025

Cellulose Xanthate–alginate Beads from Empty Palm Fruit Bunches: Synthesis, Characterization, and Application in Remazol Red Dye Degradation

Dedi Teguh[1*], Sri Rahayu Widyaningrum[1], Nita Pita Sari[1], Vida Elsyana[1], Livia Rhea Alvita[1], Adityas Agung Ramandani[2]

[1] Department of Industrial Chemical Engineering Technology, Lampung State Polytechnic, 10 Soekarno–Hatta Street, 35141 Bandar Lampung, Indonesia
[2] Department of Chemical Engineering and Materials Science, Yuan Ze University, 135 Yuandong Rd., 320 Taoyuan City, Taiwan
[*] Corresponding author, e-mail: dediteguh@polinela.ac.id

Received: 16 September 2025, Accepted: 04 December 2025, Published online: 15 December 2025

Abstract

Alginate has been extensively employed as a biomaterial, but its practical applications are constrained by inherent drawbacks such as limited solubility, structural instability, brittleness, and inadequate mechanical strength. Empty palm fruit bunches (EPFB), an abundant lignocellulosic residue rich in cellulose, represent a renewable precursor for the synthesis of cellulose xanthate. In the present study, cellulose xanthate–alginate composite beads were fabricated *via* structural modification and intermolecular interactions to overcome the intrinsic limitations of alginate. The influence of NaCl as a porogen was investigated, and the applicability of the beads in the degradation of remazol red textile dye was evaluated. Beads were prepared using a mass ratio of alginate to cellulose xanthate of 1:3, with NaCl incorporated at concentrations of 3, 6, and 9% (w/v). Characterization techniques included Fourier transform infrared spectroscopy, optical microscopy, and scanning electron microscopy-energy dispersive X-ray spectroscopy analysis. This study demonstrated that increasing NaCl concentration up to 9% enhanced the porosity and swelling capacity to 80% and 48.50%, respectively. Application tests revealed that TiO_2/cellulose xanthate–alginate beads achieved a maximum degradation efficiency of 85.59% for Remazol Red under UV irradiation with 0.8 g TiO_2. These findings highlight the potential of EPFB-derived cellulose xanthate–alginate beads as eco-friendly materials for textile dye wastewater treatment.

Keywords

alginate, beads, cellulose xanthate, empty palm fruit bunches, Remazol Red, TiO_2

1 Introduction

The palm oil industry plays a significant role in the global vegetable oil market but also generates large quantities of lignocellulosic waste. One of the major residues is empty palm fruit bunches (EPFB), which account for about 23% of each ton of fresh fruit bunches (FFB) processed [1]. The composition of EPFB is dominated by cellulose, hemicellulose, and lignin, with cellulose being the major component that supports its use as a raw material for value-added products. As a natural polysaccharide, cellulose is abundant, environmentally friendly, non-toxic, and extensively utilized in multiple industrial fields. Structurally, cellulose consists of linear chains of β-(1→4)-linked D-glucose units, with reactive hydroxyl groups distributed along the backbone [2]. These hydroxyl groups form strong intra- and intermolecular hydrogen bonds, contributing to cellulose's rigidity and insolubility in water and most organic solvents [3]. To overcome these drawbacks and broaden its applications, cellulose is often chemically modified. One such derivative, cellulose xanthate, is produced through xanthation, which disrupts hydrogen bonding and improves solubility [4].

Cellulose xanthate has been reported to exhibit superior crystallinity, enhanced thermal stability, and reduced flammability compared to native cellulose, rendering it more suitable for advanced functional materials [5]. In parallel, alginate has attracted increasing interest as a natural anionic polysaccharide derived from the cell walls of brown algae. It is composed of mannuronic and guluronic acid residues and exists mainly in the form of alginic acid or its sodium salt, sodium alginate (SA) [6].

Cite this article as: Teguh, D., Widyaningrum, S. R., Sari, N. P., Elsyana, V., Alvita, L. R., Ramandani, A. A. "Cellulose Xanthate–alginate Beads from Empty Palm Fruit Bunches: Synthesis, Characterization, and Application in Remazol Red Dye Degradation", Periodica Polytechnica Chemical Engineering, 69(4), pp. 510–524, 2025. https://doi.org/10.3311/PPch.42243

The polymer chain contains abundant hydroxyl and carboxyl groups that provide reactive sites for ionic interactions and crosslinking [6]. Overall, the binding behavior of alginate toward heavy metals is influenced by various parameters, including temperature, ionic strength, and the presence of competing ions. These factors play crucial roles and have been extensively examined by different research groups to deepen the understanding of how alginate-based materials interact with heavy metal ions [7, 8].

The detrimental effects of Remazol Red on human health have been well-documented in recent toxicological assessments. Remazol Red, a reactive azo dye widely utilized in textile industries, exhibits high chemical stability and resistance to biodegradation, enabling its persistence in environmental and biological systems. Upon exposure, this dye can undergo metabolic reduction to form aromatic amines, many of which are classified as mutagenic and carcinogenic compounds. Prolonged dermal contact or inhalation has been associated with skin irritation, allergic dermatitis, respiratory distress, and cytotoxic responses in epithelial tissues. Remazol Red is considered a significant public health concern, particularly for occupationally exposed workers in textile and dyeing facilities as well as for communities residing near industrial effluent discharge points. Therefore, comprehensive monitoring and effective treatment of Remazol Red contamination are crucial to minimize its health impact.

Alginate is recognized as a low-cost and effective adsorbent, capable of removing heavy metals, synthetic dyes, pesticides, antibiotics, and other pollutants from aqueous environments [9]. However, the direct application of natural alginate is restricted by drawbacks such as limited solubility, low viscosity, brittleness, poor elasticity, and weak mechanical properties, all of which hinder its performance in environmental applications [10]. To address these challenges, the combination of alginate with functionalized cellulose derivatives offers an attractive strategy for producing composite biomaterials with improved structural and functional properties.

Cellulose xanthate–alginate composites can be fabricated into bead-shaped structures using the ionic gelation method. This technique involves the crosslinking of alginate guluronate residues with divalent cations such as Zn^{2+}, resulting in hydrogel networks with tunable properties [11]. Beads provide significant advantages over flakes or films because of their spherical morphology, uniform particle size distribution, higher surface area, and improved mass transfer properties. These characteristics make bead-shaped composites particularly effective for adsorption processes in water and wastewater treatment. The adsorption performance of biopolymer-based beads can be further enhanced by incorporating pore-forming agents (porogens) to generate highly porous structures. Among various porogens, NaCl is widely used due to its ability to create interconnected pores, increase specific surface area, and improve adsorption capacity.

Compared to other porogens, NaCl is abundant, inexpensive, and easily to removable the final product [12]. The use of NaCl as a porogen therefore provides a cost-effective and efficient means of tailoring the textural properties of bio composites for environmental applications. Indonesia, as one of the world's largest producers of palm oil and marine biomass, possesses abundant EPFB and alginate resources. Nevertheless, these materials have not been optimally utilized to produce advanced functional composites. The transformation of cellulose obtained from EPFB into cellulose xanthate, followed by its combination with alginate to produce bead-like bio composites, offers a sustainable strategy for biomass utilization.

Such materials are biodegradable, biocompatible, and environmentally friendly, while offering enhanced adsorption performance compared with conventional adsorbents. Specifically, their high surface area and porosity make them highly effective for removing synthetic dyes, such as Remazol Red, from textile wastewater, a pollutant of growing environmental concern. Therefore, the objective of this study is to synthesize and characterize cellulose xanthate–alginate beads prepared *via* ionic gelation with NaCl as a porogen, and to evaluate their adsorption for the removal of Remazol Red dye from aqueous solutions. This work aims to provide sustainable and efficient beads derived from local renewable resources, with potential applications not only in wastewater treatment but also in drug delivery, agricultural media, and other functional biomaterial systems. Xanthate-derived materials have been increasingly explored for dye removal and degradation due to their strong affinity toward metal ions and positively charged dye molecules. The xanthate functional group $\left(-OCS_2^-\right)$ provides numerous active sites capable of forming stable complexes, enabling effective adsorption of various anionic and cationic dyes. Several studies have reported that cellulose xanthate, starch xanthate, and chitosan xanthate exhibit enhanced adsorption capacities compared to their non-modified counterparts. In addition, the presence of sulfur-containing groups in xanthates can promote redox interactions that facilitate partial degradation of dye molecules, especially under oxidative or catalytic conditions.

These findings indicate that xanthate-modified biopolymers can serve as efficient, eco-friendly adsorbents for dye removal in wastewater treatment applications.

Therefore, the main goal of this study is to synthesize and characterize cellulose xanthate–alginate beads prepared *via* ionic gelation with NaCl as a porogen, and to evaluate their adsorption efficiency toward Remazol Red dye removal from aqueous solutions. The novelty of this work lies in the synergistic integration of agricultural (EPFB-derived cellulose) and marine (alginate) biopolymers to develop sustainable, bead-shaped composites with enhanced structural, thermal, and adsorption properties. This approach not only supports waste valorization but also contributes to sustainable wastewater treatment solutions.

2 Materials and methods

2.1 Material

EPFB was obtained from PT. Perkebunan Nusantara 1 Regional 7 Bekri Plantation, Central Lampung, Lampung, Indonesia. Analytical grade chemicals were exclusively used throughout this research. Reagents such as sodium hydroxide, nitric acid, chloride acid, zinc acetate, acetic acid, sulfuric acid, sodium chloride, sodium hypochlorite, carbon disulfide, ethanol were purchased from Merck (Germany), and sodium alginate was acquired from PhytoTechnology Laboratories (USA), and Remazol Red (RB 13) was acquired from Fitinline Store (IDN).

2.2 Raw material preparation

EPFB was thoroughly cleaned and sun-dried to remove surface impurities and reduce initial moisture content. The dried material was shredded into fragments of approximately 10–20 cm and subsequently ground using a disk mill to obtain a particle size of 149 µm. The resulting powder was oven-dried at 90 °C for 24 h to ensure complete removal of residual moisture prior to further processing.

2.3 Isolation of α-cellulose from empty palm fruit bunches

A total of 75 g of EPFB powder was treated with 1 L 3.5% HNO_3 containing 10 mg $NaNO_2$ at 90 °C for 120 min, subsequently filtered and rinsed until reaching a neutral pH. The residue was subsequently treated with 750 mL 2% NaOH and 2% Na_2SO_3 at 50 °C for 60 min, filtered, and washed. Bleaching was performed using 250 mL 1.75% NaOCl at 70 °C for 30 min, and the residue was washed to neutral pH. Purification was then carried out with 500 mL 17.5% NaOH at 80 °C for 30 min, followed by washing, and further bleaching with 500 mL 10% H_2O_2 at 60 °C for 15 min. The obtained α-cellulose was washed, oven-dried at 60 °C and stored in a desiccator. The cellulose yield (%) was calculated using the following Eq. (1):

$$\text{Cellulose yield}(\%) = M_s / M_b \times 100, \tag{1}$$

where M_s is the mass of α-cellulose obtained (g) and M_b is the initial mass of EPFB powder (g) [13].

2.4 Cellulose xanthate preparation

Isolated cellulose (5 g) was treated with 40 mL 20% (w/v) NaOH for 3 h, filtered, and aged for 60 h at ambient temperature. The alkali cellulose formed was reacted with 2.5 mL of CS_2, and the mixture was homogenized at 150 rpm and 25 °C for 3 h to yield cellulose xanthate. Subsequently, 30 mL of 6% (w/v) NaOH solution was added to the suspension [14].

2.5 Beads shaping

A total of 0.5 g of SA was dissolved in 12.5 mL of demineralized water, followed by the addition of several drops of CH_3COOH until completely dissolved [14], then cellulose xanthate (4.5 g) was added with an alginate-to-cellulose xanthate mass ratio (w/w) of 1:3. NaCl served as the porogen at concentrations of 3, 6, and 9%, resulting in formulations CXA-1, CXA-2, and CXA-3. Beads produced without NaCl were referred to as CXA-0.

Homogenized mixtures were dropped through an 18G needle into 100 mL 5% (w/v) zinc acetate solution and allowed to rest for 24 h. The beads formed were filtered, rinsed with distilled water, shaken at 150 rpm for 48 h, soaked for another 24 h, and finally dried at 37 °C for 5 h. The same method was adopted for CXA-1, CXA-2, and CXA-3. The formation process of cellulose xanthate–alginate beads is summerized in Fig. 1.

2.6 Lignocellulose content analysis

Lignocellulosic analysis was carried out on both the EPFB samples and the isolated cellulose samples (α-cellulose). The determination of lignocellulosic composition in EPFB was performed through sequential fractionation based on the Chesson's method [15].

A mixture of 1 g EPFB powder and 150 mL distilled water was heated at 100 °C for 2 h in a water bath. After filtration, the residue was washed thoroughly with hot water, dried in an oven, and its mass was recorded. Subsequently, the residue was treated with 150 mL 0.5 M H_2SO_4 and refluxed at 100 °C for 2 h. The sample was filtered and washed until a neutral pH was reached, then oven-dried to a constant mass. The obtained residue was further soaked in 10 mL

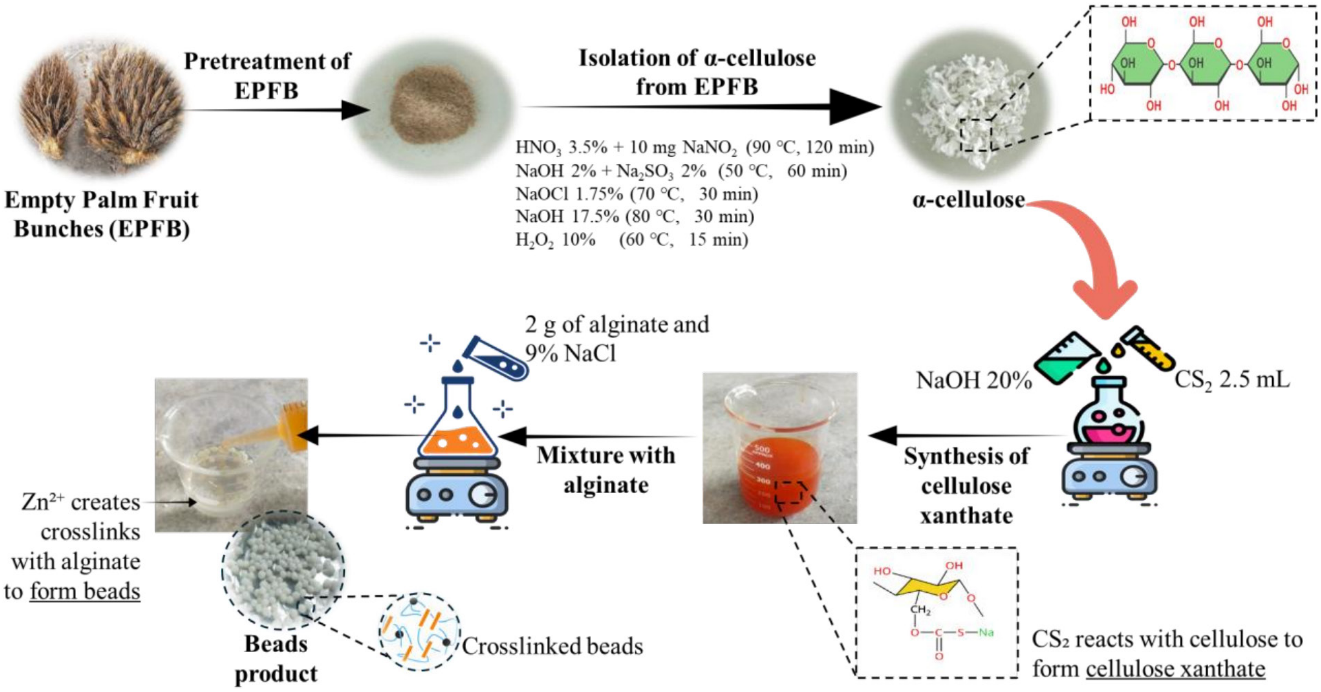

Fig. 1 Schematic representation of the formation process of cellulose xanthate–alginate beads

72% H_2SO_4 at room temperature for 4 h. The mixture was then diluted with 150 mL 0.5 M H_2SO_4, the reaction mixture underwent reflux for 2 h before being filtered. The resulting residue was neutralized through washing and dried in an oven until a constant mass was reached. The solid fraction was subsequently ashed and weighed, and the percentages of lignocellulosic components were determined according to standard calculation Eqs. (2) to (5):

$$\%\ \text{HWS} = \frac{a-b}{a}\times 100, \tag{2}$$

$$\%\ \text{Hemicellulose} = \frac{b-c}{a}\times 100, \tag{3}$$

$$\%\ \text{Lignin} = \frac{d-e}{a}\times 100, \tag{4}$$

$$\%\ \text{Cellulose} = \frac{c-d}{a}\times 100, \tag{5}$$

where *a* denotes the initial mass of the biomass sample (g), *b* represents the residue mass after hot water reflux (g), *c* corresponds to the residue mass obtained after reflux with 0.5 M H_2SO_4 (g), *d* indicates the residue mass after treatment with 72% H_2SO_4 followed by dilution (g), and *e* refers to the ash content of the residue (g).

2.7 Porosity and swelling analysis

Bead porosity was assessed by immersing samples in 5 mL ethanol (V_1) for 24 h. The system volume after immersion was designated V_2. Once the entrapped solvent within bead pores was removed, the residual ethanol was quantified as V_3. The solvent entrapped within the bead pores was then removed, and the remaining ethanol volume in the cylinder was measured as V_3. The porosity was calculated according to Eq. (6) [16]:

$$\text{Porosity}\left(\%\right) = \frac{V_1 - V_3}{V_2 - V_3}\times 100. \tag{6}$$

Bead swelling was evaluated by immersing 50 mg of beads in 20 mL of distilled water for 24 h. After immersion, the beads were weighed, and the swelling ratio was calculated using Eq. (7):

$$\text{Swelling} = \frac{W_t - W_0}{W_0}\times 100\%, \tag{7}$$

where W_t is the bead mass after immersion, and W_0 is the initial bead mass prior to immersion.

2.8 Morphology analysis

The surface morphology and elemental composition of cellulose xanthate-alginate beads were characterized using Scanning electron microscopy-energy dispersive X-ray spectroscopy (SEM-EDX) analysis (SEM ZEISS EVO MA 10).

2.9 Size analysis

Beads in wet, dry, and swollen forms were analyzed under an optical microscope, and the corresponding diameters and pore dimensions were measured using ImageJ image-processing software [17].

2.10 Preparation of TiO_2/cellulose xanthate–alginate beads

TiO_2 powder was weighed in varying amounts (0, 0.4, 0.6, and 0.8 g) and dispersed in 200 mL of demineralized water, followed by stirring for 30 min to ensure uniform suspension. Subsequently, alginate–cellulose xanthate was incorporated at a mass ratio of 1:3. To introduce porosity, 2 g NaCl was added as a porogen, and the mixture was stirred until homogeneous. The resulting solution was then extruded dropwise through a syringe needle into 100 mL 5% (w/v) zinc acetate solution, allowing beads formation *via* ionic crosslinking. The TiO_2/cellulose xanthate-alginate beads obtained were left to stand for 24 h to complete gelation, then filtered and thoroughly washed with demineralized water until a neutral pH was achieved. Finally, the beads were oven-dried at 37 °C for 5 h to obtain the final product.

2.11 Determination of the maximum absorption wavelength of Remazol Red

The Remazol Red solution was prepared at a concentration of 10 ppm. Prior to use, the solution pH was carefully adjusted to pH 6.0. The adjustment was performed by the incremental addition of either 0.1 M HCl or 0.1 M NaOH, depending on whether the initial pH needed to be lowered or raised. Each addition was followed by gentle stirring and continuous monitoring with a calibrated pH meter to ensure accurate and stable pH adjustment without overshooting the target value. The maximum absorption wavelength was then determined by scanning the solution with a UV–Vis spectrophotometer over the range of 400–700 nm. The wavelength corresponding to the highest absorbance was designated as the λ_{max}.

2.12 Preparation of the calibration curve for Remazol Red

To establish a calibration curve, Remazol Red standard solutions (2, 4, 6, 8, and 10 ppm) were examined by UV–Vis spectrophotometry at 520 nm. A linear regression of absorbance versus concentration was performed, yielding the equation $y = ax + b$.

2.13 Photocatalytic degradation of Remazol Red using TiO_2/cellulose xanthate-alginate beads

The photocatalytic degradation experiments were conducted by placing 5 g TiO_2/cellulose xanthate-alginate beads into 50 mL 10 ppm Remazol Red solution. Additional TiO_2 was incorporated with varying masses (0, 0.4, 0.6, and 0.8 g). The mixtures were first kept in the dark by wrapping the beakers with aluminum foil for 60 min to establish adsorption–desorption equilibrium. Afterward, the suspensions were irradiated with UV light (15 W lamp) positioned 10 cm above the solution surface for 180 min [15]. The residual concentration of Remazol Red was analyzed using a UV–Vis spectrophotometer at 520 nm. The photocatalytic degradation efficiency was calculated using Eq. (8):

$$\%\ \text{Degradation} = \left(\frac{X_0 - X_t}{X_0} \right) \times 100\%, \tag{8}$$

where X_0 represents the initial dye concentration, and X_t denotes the final concentration either after dark equilibration or after UV irradiation.

3 Results

3.1 Lignocellulose contents

Fig. 2 shows the lignocellulosic composition of raw EFPB biomass and the isolated *α*-cellulose fraction. A clear increase in cellulose content was observed after isolation, while hemicellulose and lignin decreased significantly. These results confirm the effectiveness of the isolation method in enriching cellulose, consistent with previous reports [18–20].

Fig. 2 presents the comparison of lignocellulosic components between raw material EPFB and *α*-cellulose EPFB. Based on the data in Fig. 2, the lignocellulosic analysis of raw EPFB showed the percentages of hot-water-soluble (HWS), hemicellulose, cellulose, and lignin were 1.28%, 29.08%, 41.35%, and 28.29%, respectively. The HWS content in raw EPFB was relatively low (<2%)

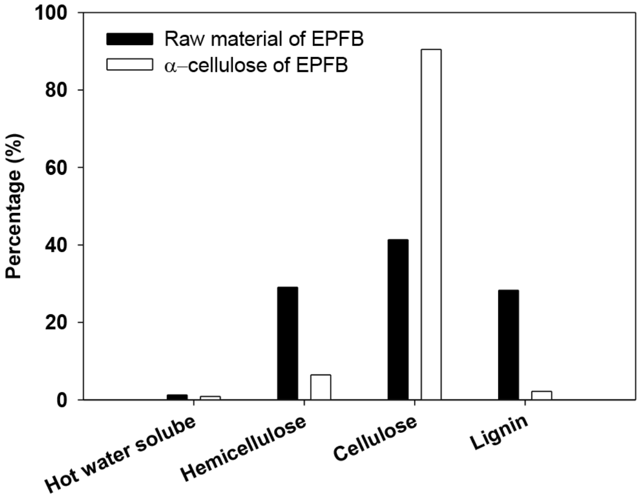

Fig. 2 Comparison of lignocellulosic components between raw material EPFB and *α*-cellulose EPFB

and did not show a significant change after the isolation process. This indicates that HWS compounds, such as simple sugars, extractives, and phenolic substances, contribute a minor fraction to the overall composition of EPFB. In contrast, the hemicellulose content in raw EPFB was relatively high (29.08%), but its proportion decreased markedly to 6.45% after the isolation process. This reduction suggests that hemicellulose, being an amorphous component, is more susceptible to hydrolysis and removal during the delignification process [21].

The most significant increase was observed in the cellulose component, which constitutes the major fraction of EPFB. In its untreated form (lignocellulosic composition), EPFB generally contains around 30–50% cellulose, depending on the method and sample conditions [22]. In this study, the cellulose content in raw EPFB reached 41.35%; however, after the isolation process, it more than doubled, reaching 90.46%. This finding demonstrates that the isolation process effectively removed most of the lignin and hemicellulose binding the cellulose structure, resulting in highly purified cellulose.

High levels of α-cellulose have previously been reported in oil palm empty fruit bunches (OPEFB) after optimized delignification processes. For instance, α-cellulose contents exceeding 94% in dissolving pulp derived from OPEFB were obtained through alkali treatment and bleaching [23] while values ranging between 88% and 94% have also been reported under optimized condition [19]. These findings confirm that OPEFB can yield high-purity α-cellulose, making it suitable for advanced material applications. Meanwhile, lignin, as the main structural component of plant cell walls that functions to protect and reinforce the cellulose matrix, exhibited a drastic reduction. In raw EPFB, the lignin content reached 28.29%; however, after the isolation process, it decreased to 2.21%. This significant reduction indicates the effectiveness of the delignification process in dissolving the hydrophobic and complex nature of lignin, thereby producing α-cellulose with an exceptionally low lignin content.

To isolate α-cellulose from raw EPFB, a delignification process was carried out using HNO_3 and $NaNO_2$. The purpose of this step was to convert lignin into water-soluble nitrolignin, which appears yellowish-brown due to the cleavage of chromophore groups in lignin and hemicellulose [24]. Following delignification, a swelling process was performed using NaOH and Na_2SO_3 to dissolve both lignin and hemicellulose by breaking the hydrogen and oxygen bonds in the phenolic OH groups of lignin, thereby disrupting the linkage between lignin and cellulose [25].

To enhance the whiteness of cellulose (bleaching), NaOCl solution was applied. However, the cellulose obtained at this stage still consisted of α-cellulose, β-cellulose, and γ-cellulose. Therefore, the separation of β-cellulose and γ-cellulose was conducted using 17.5% NaOH solution. Under strong alkaline conditions, β-cellulose and γ-cellulose, which are composed of shorter cellulose chains, readily dissolve, while α-cellulose, which has longer polymer chains, remains insoluble and precipitates [26]. During the isolation process, the resulting α-cellulose exhibited a slightly brownish-white color. To obtain a brighter white α-cellulose, an additional bleaching step was conducted using H_2O_2 solution. The overall process yielded 30.25% α-cellulose isolated from raw EPFB.

3.2 Shape, size and porosity of beads

The diameter measurements presented in Table 1 show clear dimensional differences among CXA bead formulations in both wet and dry conditions. CXA-3 exhibited the largest wet diameter (3.68 ± 0.50 mm), followed by CXA-1 (2.95 ± 0.04 mm), CXA-2 (2.75 ± 0.05 mm), and CXA-0 (2.50 ± 0.22 mm). After drying, all samples experienced size reduction, with final diameters ranging from 2.10 ± 0.15 mm to 2.73 ± 0.05 mm. The highest shrinkage was observed in CXA-3, decreasing from 3.68 mm to 2.73 mm, while the smallest dimensional change occurred in CXA-1 (2.95 mm to 2.65 mm). These results indicate that although CXA-3 initially formed the largest gel matrix, it was also more susceptible to contraction during dehydration.

The diameter of wet and dry beads was quantified using ImageJ software [17] (Fig. 3). In addition, Fig. 4 presents the morphology of dried beads, where CXA-0 samples appeared compressed, in contrast to the other formulations that predominantly displayed spherical geometry.

The addition of NaCl as a porogen influenced both the swelling properties and the bead diameter. Fig. 5 presents the graph of changes in bead diameter and mass after immersion in distilled water for 24 h. The swelling properties of the beads ranged from 41.50% to 78.80%, whereas the changes in bead diameter were between 34.50%

Table 1 Wet and dry diameters of cellulose xanthate–alginate (CXA) beads with different variations

Beads variation	Diameter (mm)	
	Wet	Dry
CXA-0	2.50 ± 0.22	2.10 ± 0.15
CXA-1	2.95 ± 0.04	2.65 ± 0.02
CXA-2	2.75 ± 0.05	2.51 ± 0.16
CXA-3	3.68 ± 0.50	2.73 ± 0.05

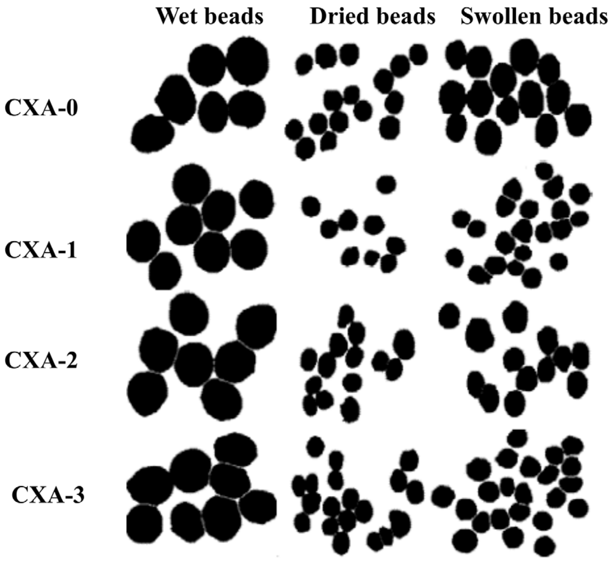

Fig. 3 Visualization and analysis of bead diameter in wet, dry and swollen states

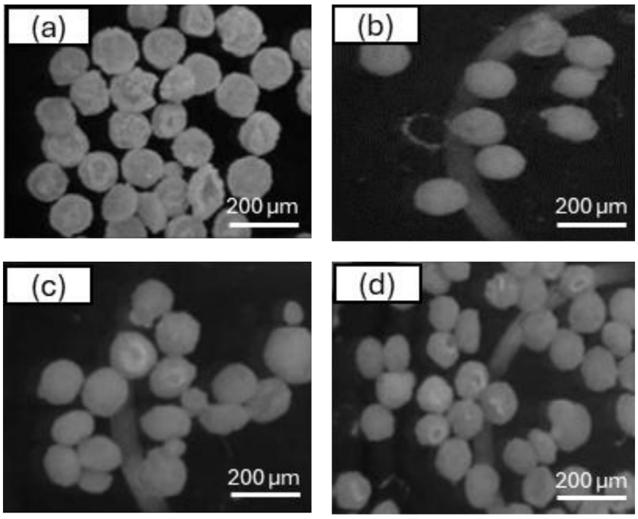

Fig. 4 Optical microscopy images of dried beads: (a) CXA-0; (b) CXA-1; (c) CXA-2; (d) CXA-3

and 41.10%. Both swelling properties and bead diameter increased with higher NaCl concentrations. This phenomenon can be attributed to the Na^+ and Cl^- ions from NaCl, which increase the osmotic pressure within the solution during bead formation [27]. The osmotic pressure difference between the bead interior and the immersion medium (distilled water) drives water molecules into the bead structure. Consequently, the beads absorb more water and exhibit enhanced swelling capacity. NaCl acts as a porogen by generating voids or pores within the polymer network during drying and rehydration [28]. At higher NaCl concentrations, a greater number of pores are formed, providing more space for water uptake, which in turn results in increased bead diameter after immersion.

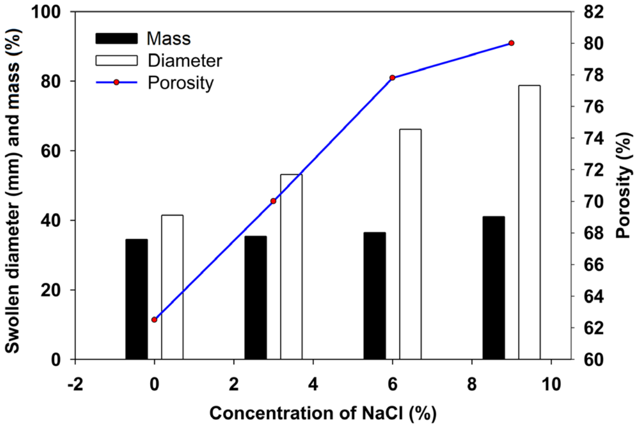

Fig. 5 Effect of NaCl concentration on the diameter, mass and porosity of swollen beads

The addition of NaCl as a porogen significantly influenced the porosity of the beads. An increase in NaCl concentration led to greater porosity and expansion of the polymer chain spacing, which facilitated water penetration into the bead matrix [27]. As shown in Fig. 5, the porosity of the beads increased proportionally with NaCl concentration. Beads CXA-2 and CXA-3 exhibited higher porosity values (77.80% and 80%, respectively) compared to CXA-1 (70%), whereas CXA-0 demonstrated the lowest porosity of 62.50%.

The increase in NaCl concentration was found to significantly influence the porosity of the resulting beads. NaCl acts as a porogen, functioning as a pore-forming agent through the salt leaching mechanism [29, 30]. During bead formation, NaCl crystals are dispersed within the polymer matrix. When the beads are immersed in water or a solvent medium, the salt crystals dissolve, leaving behind empty voids within the polymer network, thus producing a porous structure. A higher NaCl concentration generates more voids, thereby contributing to an overall increase in porosity [31, 32]. In addition, Na^+ and Cl^- ions in solution further enhance osmotic pressure during gelation. Elevated osmotic pressure promotes water diffusion into the polymer matrix, enlarging the interchain spacing and generating pores with greater dimensions.

This observation is consistent with the findings of Feng and Wang [29] who demonstrated that electrolyte ions can modulate the swelling behavior of hydrogels *via* ionic interactions, thereby improving water uptake and the development of internal porosity. Consequently, increasing NaCl concentration not only raises the number of pores but also facilitates the formation of larger pore sizes, as reflected in higher porosity values. However, a plateau effect is often observed at excessively high NaCl concentrations. Under such conditions, although pore numbers increase, partial collapse of cavities or compaction of the polymer structure may occur due to excessive ionic interactions, preventing further significant porosity enhancement [33].

Overall, increasing NaCl concentration has been demonstrated to improve bead porosity through a combined mechanism of salt leaching and osmotic pressure enhancement, directly contributing to higher swelling capacity and enlarged bead diameter. These findings are consistent with recent reports highlighting the role of inorganic salts as porogenic agents in various porous polymer systems for biomedical, pharmaceutical, and material engineering applications [28, 32, 33].

3.3 Characteristics of cellulose xanthate-alginate beads

3.3.1 Fourier transform infrared analysis

The Fourier transform infrared (FTIR) (Agilent Carry 630) spectrum provides essential insights into the chemical structure modifications occurring during the conversion of cellulose into cellulose xanthate and the subsequent formation of hybrid beads.

FTIR spectra of raw EPFB (I. spectra of Fig. 6) confirmed the presence of functional groups characteristic of lignocellulosic biomass. A broad O–H stretching band at 3280 cm^{-1} indicated hydroxyl groups from cellulose, hemicellulose, and lignin, while the peak at 2922 cm^{-1} was assigned to aliphatic C–H stretching. Absorptions at 1725–1740 cm^{-1} and 1654 cm^{-1} correspond to carbonyl groups of hemicellulose and lignin, respectively. Distinct aromatic lignin features were observed at 1600, 1510, and 1460 cm^{-1}. Meanwhile, the band at 1030–1050 cm^{-1} verified C–O–C linkages of cellulose and hemicellulose, and a weak signal at 894–900 cm^{-1} reflected β-1,4-glycosidic bonds. These findings align with previously reported FTIR patterns of untreated EFB biomass [34, 35].

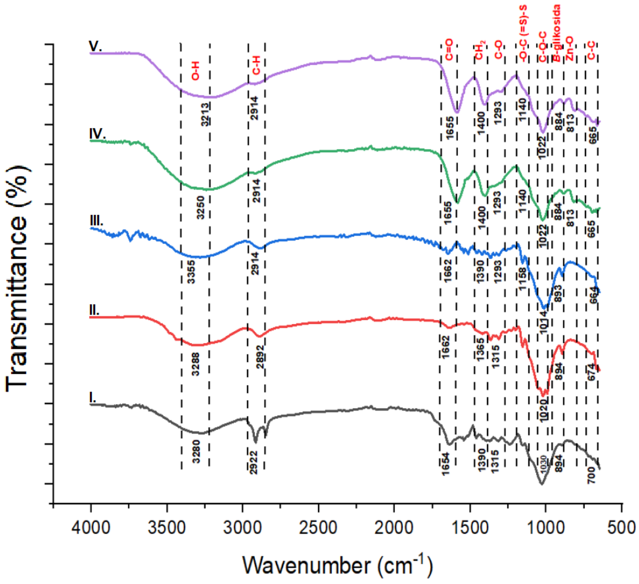

Fig. 6 FTIR spectra of: I. EPFB; II. α-cellulose; III. cellulose xanthate; IV. CXA-0; V. CXA-3

The FTIR spectrum of α-cellulose (II. spectra of Fig. 6) revealed that, following delignification and alkalization, the characteristic bands at 1730 cm^{-1} (hemicellulose) and 1510 cm^{-1} (lignin) either diminished or disappeared, indicating the effective removal of non-cellulosic components. The absorption band at 3288 cm^{-1} corresponds to O–H stretching vibrations, confirming the abundance of hydroxyl groups and the presence of both intra- and intermolecular hydrogen bonding, which are crucial for the crystalline properties of cellulose [35]. This observation further supports the reduction of hemicellulose and lignin after the purification steps.

The peak at 2892 cm^{-1} is attributed to aliphatic C–H stretching of methyl and methylene groups in glucose residues. An additional band observed at 1662 cm^{-1} is associated with H–O–H bending of adsorbed water, commonly detected in hygroscopic materials such as cellulose. Moreover, the absorptions at 1365 cm^{-1} (CH_2 scissoring) and 1315 cm^{-1} (C–H bending) reflect deformations of methyl and methylene groups and are frequently employed as indicators of cellulose crystallinity [36]. Finally, the strong band at 1020 cm^{-1}, corresponding to C–O and C–O–C stretching of glycosidic linkages, confirms the presence of glucose units within the polysaccharide backbone and highlights the preservation of cellulose's polysaccharide structure after purification [37].

The absence of a carbonyl peak around 1730 cm^{-1} indicates the low content of hemicellulose and lignin, thereby confirming the high purity of α-cellulose [38]. Scientifically, the presence of strong –OH absorption bands reflect the hydrophilic nature of cellulose and its potential to form extensive inter- and intramolecular hydrogen bonding. The characteristic band observed at 894 cm^{-1} verifies the presence of β-glycosidic linkages, a defining feature of cellulose polymers that distinguishes them from hemicellulose and lignin [39]. Collectively, the spectrum demonstrates that the primary cellulose backbone was successfully preserved after isolation, while also highlighting the typical polysaccharide characteristics of lignocellulosic biomass.

FTIR analysis of cellulose xanthate (III. spectra of Fig. 6) revealed characteristic absorption bands confirming the successful xanthation process. The broad band at 3355 cm^{-1} corresponds to O–H stretching vibrations, indicating the presence of hydroxyl groups and both intra- and intermolecular hydrogen bonding. The variation in band intensity suggests that part of the –OH groups were substituted by xanthate functionalities [14]. The absorption peak at 1662 cm^{-1} is attributed to H–O–H bending vibrations of adsorbed water molecules, while the band at 1365 cm^{-1} reflects CH_2 deformation and O–H bending, which typically shift upon chemical modification. A signal near 893 cm^{-1} remains visible, confirming that the β-1,4-glycosidic linkages of cellulose are preserved after xanthation. Furthermore, previous studies reported that the introduction of xanthate groups is evidenced by new or intensified absorptions within the range of 1200–1000 cm^{-1} (C–O–C, C=S), the C–S stretching band at 1050–1020 cm^{-1}, and the characteristic S–C–S vibrations between 800–900 cm^{-1} [38]. In addition, the spectrum displays a distinct signal at 2177 cm^{-1}, which may be associated with residual CS_2 employed during the xanthation reaction. Collectively, these FTIR results provide qualitative evidence that cellulose was successfully modified into cellulose xanthate.

FTIR spectra of CXA-0 beads without the addition of porogen/NaCl (IV. spectra of Fig. 6) exhibits a superposition of cellulose xanthate and alginate signals. From alginate, the characteristic asymmetric and symmetric stretching of carboxylate (–COO$^-$) groups are observed at 1600–1655 cm^{-1} and 1400–1425 cm^{-1}, particularly when bound ionically with Zn^{2+}/Ca^{2+}. In the range of 1020–1090 cm^{-1}, the C–O band of alginate overlaps with the C–S stretching of xanthate. The disappearance or shift of the carbonyl peak around 1730 cm^{-1} further confirms the predominance of carboxylate groups over ester functionalities. Similar FTIR patterns have been reported for alginate–cellulose xanthate beads, where such spectral features are attributed to ionic crosslinking (M^{2+}–alginate) and the presence of active xanthate moieties [14].

For CXA-3 beads (V. spectra of Fig. 6), produced with a higher NaCl/porogen content compared to CXA-0, the intensities of both the –COO$^-$ bands (1600 and 1400 cm^{-1}) and the C–S/C=S bands (1050 and 1170–1200 cm^{-1}) become more pronounced, consistent with greater exposure of active sites due to enhanced porosity. In addition, the broad O–H stretching around 3300 cm^{-1} is more evident, which can be attributed to the larger internal surface area and water retention capacity. Recent studies on CXA beads have confirmed that compositional and porogen variations enhance porosity, thereby amplifying the –COO$^-$ and C–S/C=S signals, correlating with improved cation adsorption performance.

A new band appearing at 813 cm^{-1} in both CXA-0 and CXA-3 is assigned to Zn–O bonds, indicating coordination between Zn^{2+} ions and the functional groups of alginate and xanthate. This finding supports the role of zinc acetate as a crosslinker, conferring greater structural stability to the hybrid beads [10]. Comparatively, CXA-3 beads exhibit more evident changes in the O–H stretching and polysaccharide fingerprint regions than CXA-0, suggesting a higher degree of substitution/xanthation and improved affinity toward ion and dye adsorption. These observations agree with previous reports on cellulose/xanthate-based beads applied in dye and ion removal [14].

Overall, the sequential changes in FTIR spectra across the different bead formulations provide qualitative evidence of successful cellulose transformation into cellulose xanthate, as well as the formation of hybrid beads stabilized by Zn^{2+}. This analysis further demonstrates that cellulose modification not only enhances functionality but also broadens its applicability in sustainable technologies, particularly in heavy metal adsorption and eco-friendly composite development.

3.3.2 Surface morphology

Morphological analysis using SEM provides detailed insights into the surface structure and size of the formed beads. In Fig. 7 (a) and (b), CXA-0 beads exhibit a rough, wrinkled, compact surface with no large pores. This observation is consistent with the formulation without a porogen, resulting in beads with a dense and solid structure. This occurs because no NaCl is present to act as a porogen for cavity formation, allowing the Zn^{2+}-crosslinked alginate–cellulose xanthate polymer network to form a solid structure [40, 41].

In contrast, Fig. 7 (c) and (d) show CXA-3 beads with a distinct surface morphology, characterized by

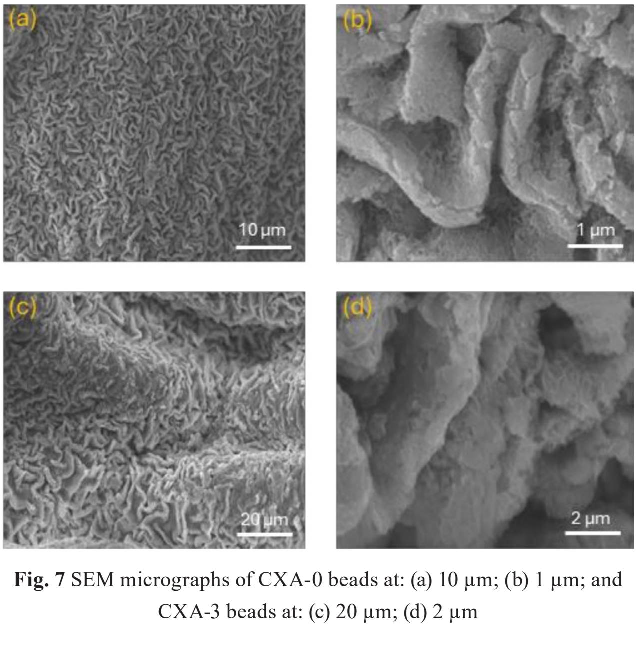

Fig. 7 SEM micrographs of CXA-0 beads at: (a) 10 µm; (b) 1 µm; and CXA-3 beads at: (c) 20 µm; (d) 2 µm

pronounced coarse folds and visible gaps. The average diameter of the beads increases, indicating that the addition of crosslinker concentration and variations in composition lead to structural expansion. The presence of surface folds and cracks suggests polymer stress relaxation during bead formation, resulting in larger internal cavities. This finding aligns with the report by Arif et al. [42], which indicates that increasing crosslinker concentration and modifying synthesis conditions can affect the polymer network density and produce a more open morphology.

The significant differences between CXA-0 and CXA-3 indicate that compositional variations affect not only bead size but also surface texture. CXA-0 beads, characterized by smaller size and finer porosity, tend to exhibit a more uniform pore distribution, whereas CXA-3 beads, with a more open surface, increased porosity with higher NaCl concentration, and larger diameters, possess a greater effective surface area. This condition can enhance interactions with target molecules, particularly in applications such as heavy metal ion adsorption or organic dye removal. Overall, SEM analysis demonstrates that compositional modifications result in notable differences in bead morphology. The porous structure of CXA-3 beads, featuring coarse folds and larger gaps, holds potential for drug delivery, biomolecule transport, and applications requiring high adsorption capacity. Consequently, bead formulation variations provide flexibility in tailoring applications based on cellulose xanthate–alginate materials.

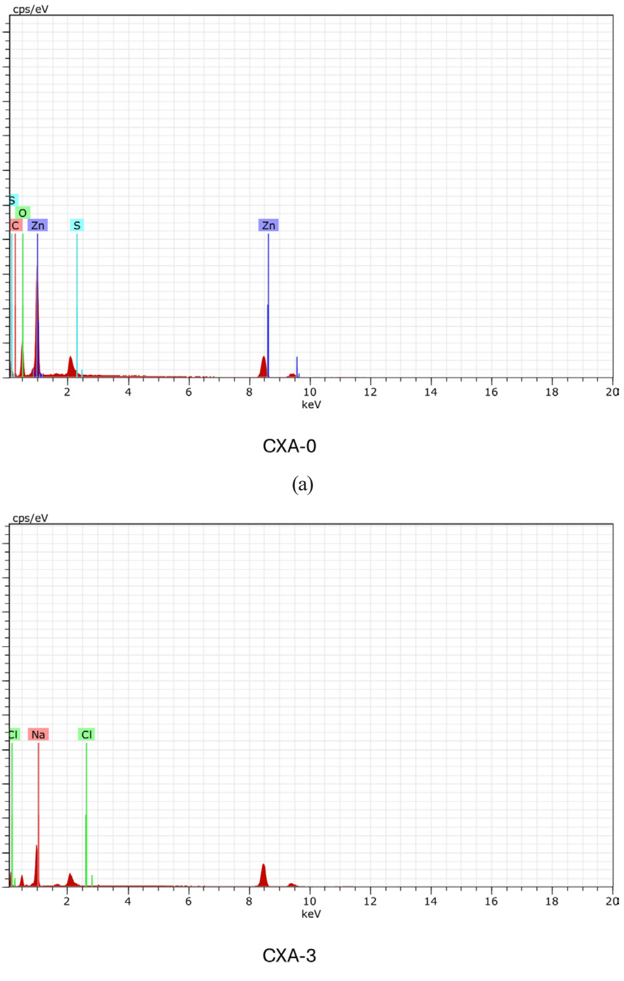

(a)

(b)

Fig. 8 EDX spectra of: (a) CXA-0 bead; (b) CXA-3 bead

3.3.3 Surface composition

EDX was employed to determine the elemental makeup of CXA-0 bead surfaces. The analysis detected C (26.38%), O (57.85%), H (4.54%), S (0.97%), and Zn (10.26%), as displayed in Fig. 8 (a).

In contrast, CXA-3 beads exhibited a high Na content of 98.15% and Cl of 1.85% (Fig. 8 (b)). In Fig. 8 (a), distinct peaks corresponding to O (0.53 keV), C (0.28 keV), S (2.31 keV), and Zn (Lα ~1.0 keV and Kα/Kβ ~8.6–9.6 keV) are observed. Oxygen and carbon are the primary components of polysaccharide-based cellulose and alginate. Sulfur originates from cellulose xanthate, as the xanthation process introduces the –CSSNa functional group. The Zn peaks indicate the presence of zinc (Zn^{2+}) derived from zinc acetate, which acts as a crosslinking agent.

The presence of Zn indicates that zinc ions successfully interacted with the carboxyl groups of alginates or the hydroxyl groups of cellulose xanthate, resulting in the formation of crosslinked bead structures. This spectrum confirms the successful crosslinking with Zn and the incorporation of xanthate elements (S) within the CXA-0 bead matrix. Meanwhile, Fig. 8 (b) displays peaks corresponding to Na (1.04 keV) and Cl (2.62 keV), in addition to the C and O peaks. The Na and Cl originate from NaCl used as a porogen during bead synthesis. The presence of Na and Cl peaks suggests that residual NaCl may remain trapped within the pores, not fully dissolved or removed during the washing process.

This phenomenon is commonly observed in the preparation of porous beads, as some salt can be retained within the pore network. The spectrum highlights the role of NaCl as a porogen agent, influencing bead porosity, size, and mechanical strength, while still leaving traces of Na and Cl elements [43]. The combined results from EDX analysis (Fig. 8 (a) and (b)) indicate that Zn successfully incorporated into the bead matrix, functioning as a crosslinker to reinforce and stabilize the bead structure. Recent studies have shown that Zn effectively enhances gel strength, modulates surface charge, and influences the release of active compounds [44]. Practically, the detection of Zn peaks (L and K lines) in the EDX spectra confirms the successful ionotropic gelation using zinc acetate. Moreover, Zn^{2+} plays a role in determining mechanical properties, water absorption, and bioactivity [45]. The presence of sulfur (S) confirms the incorporation of xanthate groups from cellulose xanthate. Meanwhile, Na and Cl signals reflect the use of NaCl as a porogen, some of which remain trapped within the beads. Overall, these EDX results validate the successful synthesis of cellulose xanthate/alginate beads crosslinked with zinc acetate and templated with NaCl, producing a stable, porous crosslinked structure with potential for controlled release and adsorption applications.

3.4 Photocatalytic activity test of TiO_2/cellulose xanthate–alginate beads on Remazol Red solution

3.4.1 Maximum wavelength of Remazol Red

At this stage, the maximum wavelength of the Remazol Red dye (RB 133) was determined. The maximum wavelength represents the region of highest absorption, corresponding to the excitation of electrons by specific energy. The determination was carried out within the wavelength range of 400–700 nm using a UV–Vis spectrophotometer. A standard Remazol Red solution (10 ppm) was scanned to identify its maximum absorption wavelength. The results indicated that the highest absorbance value (0.318) was observed at 520 nm (Fig. 9).

3.4.2 Calibration curve of Remazol Red

The standard curve of Remazol Red was established to determine the absorbance values of the dye solution and to convert absorbance into concentration, thereby enabling quantitative analysis of the degradation process. The results demonstrate a clear linear correlation between concentration and absorbance, in agreement with the Lambert–Beer law, which states that absorbance (A) is directly proportional to solution concentration (C in ppm) at a specific wavelength. The linear regression analysis yielded Eq. (9):

$$A = 0.033C - 0.0015,\ R^2 = 0.9998. \qquad (9)$$

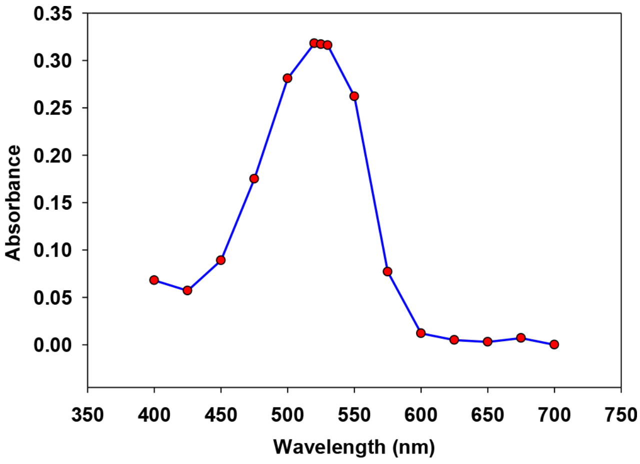

Fig. 9 Wavelength maximum of Remazol Red

This strong linearity is crucial, as it allows the absorbance values of unknown samples to be accurately projected onto the standard curve for precise concentration determination [46]. The close alignment of the experimental data points with the regression line further confirms that UV–Vis spectrophotometry at λ_{max} 520 nm is a reliable method for the quantitative analysis of Remazol Red in aqueous solutions. Hence, the established standard curve provides a robust and dependable basis for calculating the concentration of unknown Remazol Red samples.

3.4.3 Degradation test of Remazol Red solution using TiO_2/cellulose xanthate-alginate beads

The photocatalytic activity test was conducted to evaluate the degradation performance of the material toward Remazol Red solution. The experiment was carried out using a 10 ppm Remazol Red solution with cellulose xanthate–alginate beads incorporated with varying TiO_2 masses (0, 0.4, 0.6, and 0.8 g). The degradation process was assessed under two different conditions: in the dark (without UV irradiation) and under illumination (with UV irradiation). The degradation results are presented in Fig. 10.

Fig. 10 illustrates the increase in degradation percentage with the addition of TiO_2 content in the beads, under both dark and illuminated conditions (ranging from 15.06–36.02% in the dark and 42.83–85.59% under UV irradiation). This trend highlights the dual role of TiO_2 in the

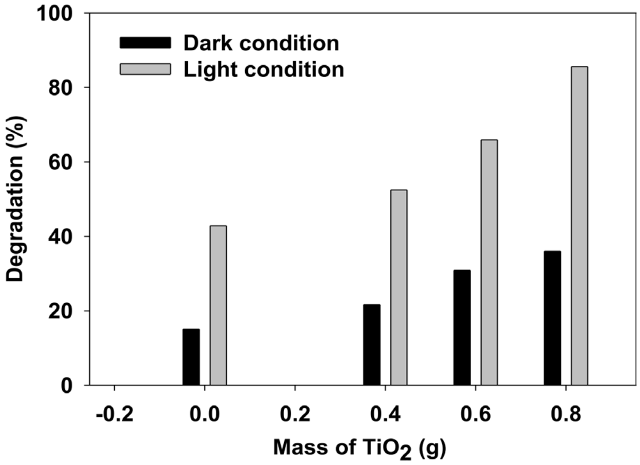

Fig. 10 The effect of TiO_2 mass in cellulose xanthate–alginate beads on the degradation percentage of Remazol Red solution under dark and illuminated conditions

integrated adsorption–photocatalysis system. Under dark conditions, the enhancement of degradation is primarily attributed to the adsorption of dye molecules onto the surface of the beads, supported by the adsorptive nature of the cellulose xanthate–alginate matrix. In contrast, under illumination, the additional photocatalytic contribution of TiO_2 – *via* electron–hole pair generation and hydroxyl radical formation – significantly accelerates the breakdown of dye chromophores [47]. This finding is consistent with previous studies reporting the synergistic effect of adsorption and photocatalysis in TiO_2 immobilized within alginate/hydrogel and cellulose-based matrices [48].

The progressive increase in degradation under dark conditions (15.06–36.02%) with higher TiO_2 loading also indicates that, beyond its photocatalytic role, TiO_2 enhances the surface area and adsorption sites within the beads. Moreover, the integration of TiO_2 with the cellulose xanthate–alginate matrix improves porosity and adsorption capacity, allowing greater dye retention, which is subsequently susceptible to degradation when exposed to light. Related studies have shown that biopolymer matrices (alginates/cellulose) act as effective supports, improving the stability and dispersion of TiO_2 particles [47].

The degradation efficiency under illumination was substantially higher (85.59%) compared to dark conditions (36.02%) at all TiO_2 loadings. The standard deviations under illumination and dark conditions are 0.0228 and 0.0196, respectively. This confirms the dominant photocatalytic contribution under light exposure (UV–Vis), where TiO_2 generates reactive oxidative radicals responsible for the rapid cleavage of azo and aromatic structures in Remazol Red [49]. Recent reports on TiO_2–alginate/hydrogel beads also demonstrate high removal efficiencies (≥80%) under irradiation, in agreement with the present findings. Overall, Fig. 10 confirms that increasing TiO_2 content in cellulose xanthate–alginate beads enhance Remazol Red degradation, with photocatalytic activity playing the dominant role under illuminated conditions, achieving up to 85.6% efficiency at a TiO_2 loading of 0.8 g. These results are consistent with recent literature on TiO_2 immobilized in alginate/cellulose matrices, which combine adsorption and photocatalysis mechanisms [50].

4 Conclusion

The isolation process of cellulose from EPFB successfully removed most of the lignin and hemicellulose, yielding α-cellulose with a recovery of 30.25% and a cellulose content of 90.46%. A direct correlation was observed between NaCl concentration and both swelling and porosity of the beads. At 9% NaCl, the maximum swelling (48.50%) and porosity (80%) were achieved. Overall, the changes observed in the FTIR spectra at each stage confirmed the successful transformation of cellulose into cellulose xanthate and the subsequent formation of hybrid beads stabilized by Zn^{2+}. Complementary SEM analysis further demonstrated that compositional modifications led to significant differences in bead morphology. The degradation test of Remazol Red solution using TiO_2/cellulose xanthate–alginate beads achieved the highest degradation efficiency of 85.59% at a TiO_2 loading of 0.8 g under UV irradiation.

Acknowledgement

The authors would like to express their gratitude to the Research and Community Service Center, Politeknik Negeri Lampung, through the Applied Research Scheme for the Fiscal Year 2025 under Grant No. 180.2.24/PL15/PP/2025.

References

[1] Mardawati, E., Febrianti, E. A., Fitriana, H. N., Yuliana, T., Putriana, N. A., Suhartini, S., Kasbawati "An Integrated Process for the Xylitol and Ethanol Production from Oil Palm Empty Fruit Bunch (OPEFB) Using *Debaryomyces hansenii* and *Saccharomyces cerevisiae*", Microorganisms, 10(10), 2036, 2022. https://doi.org/10.3390/microorganisms10102036

[2] Etale, A., Onyianta, A. J., Turner, S. R., Eichhorn, S. J. "Cellulose: A Review of Water Interactions, Applications in Composites, and Water Treatment", Chemical Reviews, 123(5), pp. 2016–2048, 2023. https://doi.org/10.1021/acs.chemrev.2c00477

[3] Acharya, S., Liyanage, S., Parajuli, P., Rumi, S. S., Shamshina, J. L., Abidi, N. "Utilization of Cellulose to Its Full Potential: A Review on Cellulose Dissolution, Regeneration, and Applications", Polymers, 13(24), 4344, 2021. https://doi.org/10.3390/polym13244344

[4] Jarvis, M. C. "Hydrogen bonding and other non-covalent interactions at the surfaces of cellulose microfibrils", Cellulose, 30(2), pp. 667–687, 2023. https://doi.org/10.1007/s10570-022-04954-3

[5] Novita, N., Budhijanto, B., Azis, M. M. "A Systematic Study on the Effect of the Xanthation Temperature on Viscose Quality", Engineering Proceedings, 67(1), 6, 2024. https://doi.org/10.3390/engproc2024067006

[6] Abka-khajouei, R., Tounsi, L., Shahabi, N., Patel, A. K., Abdelkafi, S., Michaud, P. "Structures, Properties and Applications of Alginates", Marine Drugs, 20(6), 364, 2022. https://doi.org/10.3390/md20060364

[7] Córdova, B. M., Venâncio, T., Olivera, M., Huamani-Palomino, R. G., Valderrama, A. C. "Xanthation of alginate for heavy metal ions removal. Characterization of xanthate-modified alginates and its metal derivatives", International Journal of Biological Macromolecules, 169, pp. 130–142, 2021.
https://doi.org/10.1016/j.ijbiomac.2020.12.022

[8] Córdova, B. M., Infantas, G. C., Mayta, S., Huamani-Palomino, R. G., Kock, F. V. C., Montes de Oca, J., Valderrama, A. C. "Xanthate-modified alginates for the removal of Pb(II) and Ni(II) from aqueous solutions: A brief analysis of alginate xanthation", International Journal of Biological Macromolecules, 179, pp. 557–566, 2021.
https://doi.org/10.1016/j.ijbiomac.2021.02.190

[9] Adamiak, K., Sionkowska, A. "State of Innovation in Alginate-Based Materials", Marine Drugs, 21(6), 353, 2023.
https://doi.org/10.3390/md21060353

[10] Rohmatullah, W. A. P., Yulianti, E., Khoiroh, L. M., Mahmudah, R. "Synthesis and Characterization of Alginate-Cellulose Xanthate Beads from Corn Stalk with NaCl As Porogen", Annales Bogorienses, 24(2), pp. 59–65, 2025. [online] Available at: https://ejournal.brin.go.id/annales/article/view/4281 [Accessed: 15 September 2025]

[11] Jeong, C., Kim, S., Lee, C., Cho, S., Kim, S.-B. "Changes in the Physical Properties of Calcium Alginate Gel Beads under a Wide Range of Gelation Temperature Conditions", Foods, 9(2), 180, 2020.
https://doi.org/10.3390/foods9020180

[12] Lakshmi, D. S., Radha, K. S., Castro-Muñoz, R., Tańczyk, M. "Emerging Trends in Porogens toward Material Fabrication: Recent Progresses and Challenges", Polymers, 14(23), 5209, 2022.
https://doi.org/10.3390/polym14235209

[13] Kamar, I., Yuniharni, D., Emilia, R. "Isolasi carboxymethyl cellulose (CMC) dengan memanfaatan limbah tongkos sawit sebagai pengganti CMC komersil" (Isolation of carboxymethyl cellulose (CMC) using oil palm cob waste as a substitute for commercial CMC), Inovasi Teknik Kimia, 9(1), pp. 17–23, 2024. (in Indonesian)
https://doi.org/10.31942/inteka.v9i1.9640

[14] Yulianti, E., Khoiroh, L. M., Mahmudah, R., Puspitasari, S., Himmah, F., …, Elkhooly, T. A. "Extraction of Cellulose from Bagasse for the Synthesis of Alginate: Cellulose Porous Beads", Asian Journal of Green Chemistry, 8(3), pp. 278–295, 2024.
https://doi.org/10.48309/ajgc.2024.440660.1475

[15] Datta, R. "Acidogenic fermentation of lignocellulose–acid yield and conversion of components", Biotechnology and Bioengineering, 23(9), pp. 2167–2170, 1981.
https://doi.org/10.1002/bit.260230921

[16] Eiselt, P., Yeh, J., Latvala, R. K., Shea, L. D., Mooney, D. J. "Porous carriers for biomedical applications based on alginate hydrogels", Biomaterials, 21(19), pp. 1921–1927, 2000.
https://doi.org/10.1016/S0142-9612(00)00033-8

[17] Schindelin, J., Arganda-Carreras, I., Frise, E., Kaynig, V., Longair, M., …, Cardona, A. "Fiji: ImageJ Distribution (2.14.0)", [computer program] Available at: https://fiji.sc/ [Accessed: 10 August 2025]

[18] Gegova-Dzhurkova, R., Nesheva, D., Stambolova, I., Zaharieva, K., Dzhurkov, V., Miloushev, I. "Enhanced Photocatalytic Performance under Ultraviolet and Visible Light Illumination of ZnO Thin Films Prepared by Modified Sol-Gel Method", Molecules, 29(17), 4005, 2024.
https://doi.org/10.3390/molecules29174005

[19] Hindi, S. S. "Novel Recycling, Defibrillation, and Delignification Methods for Isolating α-Cellulose from Different Lignocellulosic Precursors for the Eco-Friendly Fiber Industry", Polymers, 16(17), 2430, 2024.
https://doi.org/10.3390/polym16172430

[20] Kweon, S. W., Lee, T. J., Lee, Y. J., Seo, J. H., Kim, H. J. "High-purity cellulose extraction and cellulose acetate synthesis from paper mulberry bast fibers for sustainable material applications", Industrial Crops and Products, 235, 121824, 2025.
https://doi.org/10.1016/j.indcrop.2025.121824

[21] Susi, S., Ainuri, M., Wagiman, W., Falah, M. A. F. "High-Yield Alpha-Cellulose from Oil Palm Empty Fruit Bunches by Optimizing Thermochemical Delignification Processes for Use as Microcrystalline Cellulose", International Journal of Biomaterials, 2023(1), 9169431, 2023.
https://doi.org/10.1155/2023/9169431

[22] Nurdin, M., Abimanyu, H., Putriani, H., Setiawan, L. O. M. I., Maulidiyah, M., …, Mustapa, F. "Optimization of OPEFB lignocellulose transformation process through ionic liquid [TEA][HSO_4] based pretreatment", Scientific Reports, 11(1), 11338, 2021.
https://doi.org/10.1038/s41598-021-90891-3

[23] Nikmatin, S., Irmansyah, I., Hermawan, B., Kardiansyah, T., Seta, F. T., Afiah, I. N., Umam, R. "Oil Palm Empty Fruit Bunches as Raw Material of Dissolving Pulp for Viscose Rayon Fiber in Making Textile Products", Polymers, 14(15), 3208, 2022.
https://doi.org/10.3390/polym14153208

[24] Trisnawita, Y., Putri, E. "Sintesis dan karakterisasi karboksimetil selulosa (CMC) dari limbah tandan kosong kelapa sawit (tkks) sebagai pengganti CMC industri" (Synthesis and characterization of carboxymethyl cellulose (CMC) derived from oil palm empty fruit bunch (EFB) waste as an alternative to industrial-grade CMC), Jurnal Kimia Saintek Dan Pendidikan, 8(1), pp. 41–48, 2024. (in Indonesian)
https://doi.org/10.51544/kimia.v8i1.4656

[25] Plakantonaki, S., Zacharopoulos, N., Christopoulos, M., Kiskira, K., Markou, G., Tsakanika, L.-A., Priniotakis, G. "Upcycling industrial peach waste to produce dissolving pulp", Environmental Science and Pollution Research, 32(8), pp. 4636–4655, 2025.
https://doi.org/10.1007/s11356-025-35977-5

[26] Shaikh, H. M., Anis, A., Poulose, A. M., Al-Zahrani, S. M., Madhar, N. A., Alhamidi, A., Alam, M. A. "Isolation and Characterization of Alpha and Nanocrystalline Cellulose from Date Palm (*Phoenix dactylifera* L.) Trunk Mesh", Polymers, 13(11), 1893, 2021.
https://doi.org/10.3390/polym13111893

[27] Zheng, S., Li, Y., Shao, Y., Li, L., Song, F. "Osmotic Pressure and Its Biological Implications", International Journal of Molecular Sciences, 25(6), 3310, 2024.
https://doi.org/10.3390/ijms25063310

[28] Mokhtarzadegan, M., Mojtaba Zebarjad, S., Bahrololoom, M. E., Modarres, M. "Effect of sodium chloride as a porogen agent in mechanical properties of PLGA/HA nanocomposite scaffolds", Biomedical Physics & Engineering Express, 7(3), 035009, 2021. https://doi.org/10.1088/2057-1976/ab61c1

[29] Feng, W., Wang, Z. "Tailoring the Swelling-Shrinkable Behavior of Hydrogels for Biomedical Applications", Advanced Science, 10(28), 2303326, 2023. https://doi.org/10.1002/advs.202303326

[30] Allaf, R. M. "The effect of PEO/NaCl dual porogens in the fabrication of porous PCL membranes via a solid-state blending approach", Scientific Reports, 15(1), 454, 2025. https://doi.org/10.1038/s41598-024-84743-z

[31] Valamvanos, T. F., Dereka, X., Katifelis, H., Gazouli, M., Lagopati, N. "Recent Advances in Scaffolds for Guided Bone Regeneration", Biomimetics, 9(3), 153, 2024. https://doi.org/10.3390/biomimetics9030153

[32] González-Henríquez, C. M., Rodríguez-Umanzor, F. E., Acuña-Ruiz, N. F., Vera-Rojas, G. E., Terraza-Inostroza, C., Cohn-Inostroza, N. A., Utrera, A., Sarabia-Vallejos, M. A., Rodríguez-Hernández, J. "Fabrication and Testing of Multi-Hierarchical Porous Scaffolds Designed for Bone Regeneration via Additive Manufacturing Processes", Polymers, 14(19), 4041, 2022. https://doi.org/10.3390/polym14194041

[33] Wu, C., Zhang, H., Guo, Y., Sun, X., Hu, Z., Teng, L., Zeng, Z. "Porous Hydrogels for Immunomodulatory Applications", International Journal of Molecular Sciences, 25(10), 5152, 2024. https://doi.org/10.3390/ijms25105152

[34] Afandi, T., Sitinjak, E. M., Pratikha, R S., Nainggolan, F. "Characterization of unbleached pulp from empty fruit bunches of oil palm as a raw material for brown paper", Cellulose Chemistry and Technology, 58(5–6), pp. 541–546, 2024. https://doi.org/10.35812/CelluloseChemTechnol.2024.58.50

[35] Singhal, K., Boy, R., Abdullah, A. M., Mazeed, T., Demirel, M. C. "Engineering advanced cellulosics for enhanced triboelectric performance using biomanufactured proteins", npj Materials Sustainability, 2(1), 29, 2024. https://doi.org/10.1038/s44296-024-00035-7

[36] Salem, K. S., Kasera, N. K., Rahman, M. A., Jameel, H., Habibi, Y., Eichhorn, S. J., French, A. D., Pal, L., Lucia, L. A. "Comparison and assessment of methods for cellulose crystallinity determination", Royal Society Reviews, 52(18), pp. 6417–6446, 2023. https://doi.org/10.1039/d2cs00569g

[37] Tsaousis, P. C., Sarafidou, M., Soto Beobide, A., Mathioudakis, G. N., Filippi, K., …, Voyiatzis, G. A. "Quantification of plant biomass composition via a single FTIR absorption spectrum supported by reference component extraction/isolation protocols", Biomass Conversion and Biorefinery, 15(18), pp. 25273–25288, 2025. https://doi.org/10.1007/s13399-025-06858-1

[38] Mamudu, U., Kabyshev, A., Bekmyrza, K., Kuterbekov, K. A., Baratova, A., Omeiza, L. A., Lim, R. C. "Extraction, Preparation and Characterization of Nanocrystalline Cellulose from Lignocellulosic Simpor Leaf Residue", Molecules, 30(7), 1622, 2025. https://doi.org/10.3390/molecules30071622

[39] Hasan, M. H., Hossain, S., Rahman, M. L., Rahman, G. M. S., Khan, M. A., Mamun, M. A. A. "Effect of hydrolysis agitation and suspension drying temperature on the synthesis of crystalline cellulose from jute fiber", Carbohydrate Polymer Technologies and Applications, 10, 100769, 2025. https://doi.org/10.1016/j.carpta.2025.100769

[40] Homagai, P. L., Bhattarai, M., Radhika, K. M., Ghimire, K. N., Paudyal, H., Bhattarai, A. "Comparative study of Hg(II) biosorption performance of xanthated and charred sugarcane bagasse from aqueous solutions", RSC Advances, 12(46), pp. 29865–29877, 2022. https://doi.org/10.1039/d2ra05266k

[41] Lizundia, E., Costa, C. M., Alves, R., Lanceros-Méndez, S. "Cellulose and its derivatives for lithium ion battery separators: A review on the processing methods and properties", Carbohydrate Polymer Technologies and Applications, 1, 100001, 2020. https://doi.org/10.1016/j.carpta.2020.100001

[42] Arif, M., Javed, M., Akhter, T. "Crosslinked polymeric networks of TiO_2-polymer composites: a comprehensive review", RSC Advances, 14(46), pp. 33843–33863, 2024. https://doi.org/10.1039/d4ra06922f

[43] Jurczak, K. M., Zhang, R., Hinrichs, W. L. J., Grijpma, D. W., Schuurmann, R. C. L., de Vries, J.-P. P. M., van Rijn, P. "Porous polytrimethylenecarbonate scaffolds: Design considerations and porosity modulation techniques", Materials & Design, 250, 113588, 2025. https://doi.org/10.1016/j.matdes.2025.113588

[44] Reczkowski, J., Długosz, M., Ratajczak, M., Voelkel, A., Sandomierski, M. "Gelatin–Zinc Carrier as a New Method of Targeted and Controlled Release of Risedronate", Materials, 17(11), 2473, 2024. https://doi.org/10.3390/ma17112473

[45] Szekalska, M., Kasparavičienė, G., Bernatonienė, J., Wolska, E., Misiak, P., Markiewicz, K. H., Wilczewska, A. Z., Czajkowska-Kośnik, A., Winnicka, K. "Zinc Acetate as a Cross-Linking Agent in the Development of Enteric Microcapsules for Posaconazole", Pharmaceutics, 17(3), 291, 2025. https://doi.org/10.3390/pharmaceutics17030291

[46] Rahaman, M. H., Miah, M. P., Siam, M. M. I., Barat, M. K., Uddin, M. A. "Removal of reactive dyes-based wastewater with moringa-coated cellulose microcrystals (CMC) produced from sugarcane bagasse", Cleaner Water, 3, 100087, 2025. https://doi.org/10.1016/j.clwat.2025.100087

[47] Nguyen, B. C., Truong, T. M., Nguyen, N. T., Dinh, D. N., Hollmann, D., Nguyen, M. N. "Advanced cellulose-based hydrogel TiO_2 catalyst composites for efficient photocatalytic degradation of organic dye methylene blue", Scientific Reports, 14(1), 10935, 2024. https://doi.org/10.1038/s41598-024-61724-w

[48] Kumar, R., Ansari, M. O., Taleb, M. A., Oves, M., Barakat, M. A., Alghamdi, M. A., Al Makishah, N. H. "Integrated Adsorption-Photocatalytic Decontamination of Oxytetracycline from Wastewater Using S-Doped TiO_2/WS_2/Calcium Alginate Beads", Catalysts, 12(12), 1676, 2022. https://doi.org/10.3390/catal12121676

[49] Gatou, M.-A., Syrrakou, A., Lagopati, N., Pavlatou, E. A. "Photocatalytic TiO_2-Based Nanostructures as a Promising Material for Diverse Environmental Applications: A Review", Reactions, 5(1), pp. 135–194, 2024. https://doi.org/10.3390/reactions5010007

[50] Tan, S. N., Yuen, M. L., Ramli, R. A. "Photocatalysis of dyes: Operational parameters, mechanisms, and degradation pathway", Green Analytical Chemistry, 12, 100230, 2025. https://doi.org/10.1016/j.greeac.2025.100230